Research papers

Novel model reference-based hybrid decoupling control of multiport-isolated DC-DC converter for hydrogen energy storage system integration

Oyedotun E. Oyewole [a,*], Ali A. Abdelaziz [a], Ibrahim Abdelsalam [b], Eugene Bari [c], Khaled H. Ahmed [a]

[a] *Department of Electronic and Electrical Engineering, University of Strathclyde, Glasgow G1 1XQ, UK*
[b] *Arab Academy for Science Technology and Maritime Transport, Cairo Campus, Cairo, EG, Egypt*
[c] *Ecomar Propulsion Ltd., 32 Standard Way, Fareham PO16 8XG, UK*

ABSTRACT

Hydrogen energy storage systems (HESS) are increasingly recognised for their role in sustainable energy applications, though their performance depends on efficient power electronic converter (PEC) interfaces. In this paper, a multiport-isolated DC-DC converter, characterised by enhanced power density, reduced component count, and minimal conversion stages, is implemented for HESS applications. However, the high-frequency multiwinding transformer in this converter introduces cross-coupling effects, complicating control and resulting in large power deviations from nominal values due to step changes on other ports, which adversely impact system performance. To address this issue, a novel model reference-based decoupling control technique is proposed to minimise the error between the actual plant output and an ideal decoupling reference model, which represents the cross-coupling term. This model reference-based decoupling control is further extended into a hybrid decoupling control technique by integrating a decoupling matrix, achieving more robust decoupling across a wider operating region. The hybrid decoupling technique mathematically ensures an improved control performance, with the cross-coupling term minimised through a proportional-derivative controller. The proposed hybrid decoupling controller achieves a maximum power deviation of <3 % under various conditions, outperforming the conventional inverse decoupling matrix technique, which typically exhibits higher deviations under similar conditions. The effectiveness of the hybrid decoupling control is validated through simulations and experimental results, demonstrating significant improvements in decoupling performance.

1. Introduction

Reliable and sustainable energy production is crucial for economic growth and environmental preservation. The global energy industry has experienced substantial growth and is largely powered by fossil fuels. However, reliance on fossil fuels has led to adverse environmental impacts, including greenhouse gas emissions that contribute to climate change [1,2]. In response, there has been a global shift toward renewable energy sources such as solar and wind, which aligns with the United Nations sustainable development goals (SDGs), particularly SDG 7 (affordable and clean energy) and SDG 13 (climate action) [3]. Despite the benefits, renewable energy sources face challenges of intermittency, which complicates their integration into the power grid [4,5]. To

address this, energy storage solutions, particularly hydrogen energy storage systems (HESS), offer a promising approach [6]. As an electrochemical energy storage method, HESS provide long-term storage capabilities with high capacity compared to other energy storage elements, as shown in Table 1.

HESS are therefore emerging large-scale energy storage and power generation. These systems store surplus energy from renewable or distributed energy (DE) sources during periods of low demand and release it during peak times, thereby enhancing the efficiency and resilience of the energy system. As depicted in Fig. 1, DE sources (which could include a microgrid) supply power to the system, with the energy directed toward electrolysis through electrolysers (EL) to split water into hydrogen and oxygen. The resulting hydrogen is stored in high-pressure

Table 1
Comparison of energy storage systems [7].

Type	Category	Discharge time	Capacity	Efficiency
HESS	Electrochemical	<1000 h	<1 GW	30–45 %
Battery	Electrochemical	<5 h	<100 MW	70–85 %
Flywheels	Mechanical	<30 min	<1 MW	85–100 %
Compressed air	Mechanical	<100 h	<10 MW	45–70 %
Pumped hydro	Mechanical	<500 h	<0.8 GW	70–85 %
Superconducting magnetic	Electromagnetic	< 5 h	<5 MW	85–99 %

tanks, while the oxygen byproduct is vented to the atmosphere. The stored hydrogen can then be utilised in marine or aerospace applications. A battery (BT) system, such as a Ni-MH battery, which utilises hydrogen storage alloys and features high charge and discharge rates along with environmentally friendly characteristics, as shown in Fig. 1, provides rapid-response energy storage by absorbing excess energy from DE and supporting continuous hydrogen production if DE fails [8]. HESS operate across three main stages: hydrogen production, storage, and re-electrification [9]. Various technologies, including alkaline electrolysis, solid oxide cells, and proton exchange membranes, have been employed for the production of hydrogen [10].

The HESS is supported by several auxiliary subsystems that ensure their complete functionality, including air and hydrogen supply systems, cooling and heat exchangers, humidification systems, and power electronic converters (PEC), all of which are highly interconnected to optimise system performance [11,12]. Among these, PECs play a critical role in HESS operation. The PEC regulates the electrical input required for water splitting, controls the voltage and current levels to maintain efficiency, and prevents degradation of the EL components. As stated in [13], 12 % of the HESS losses occur in the PEC; hence, there is a need for an efficient PEC interface. Conventional HESS designs, as illustrated by the dual-converter structure in Fig. 1, often use multiple interconnected converters, leading to bulky and costly systems with increased circulating currents and poor dynamic responses [14,15]. These limitations highlight the need for converter designs that fulfil stringent HESS requirements for adequate functioning, including high conversion ratios, low current ripple, high current delivery, high efficiency, high power density, and fault tolerance [16,17]. However, designing a HESS that

satisfies these interface requirements is challenging. To address these issues, multiport converters have been explored. These converters integrate multiple converter units into a single entity, thereby reducing the number of conversion stages, component count, and control complexity [15,18].

The multiport isolated converters, such as the triple active bridge (TAB) shown in the inset of Fig. 1, have been proposed. The TAB can replace the two "converters of interest" in Fig. 1, providing ease of cascade, high voltage gain ratio, higher power density, and galvanic isolation for safety reasons compared to non-isolated configurations [19]. A multiwinding high-frequency transformer is a key component of a multiport-isolated DC-DC converter, providing voltage conditioning, voltage matching, and galvanic isolation. However, this transformer introduces coupling effects due to electromagnetic interactions between its windings, which can disrupt power flow control in the converter, leading to poor dynamic response and reduced stability [20]. This cross-coupling effect may lead to unstable hydrogen production in EL, resulting in diminished performance, lower efficiency, and energy wastage [21]. Therefore, mitigating this effect is crucial for enhancing the converter performance.

The implemented multiport-isolated DC-DC converter in HESS can be characterised as a multiple-input multiple-output (MIMO) system with inherent control challenges due to coupled control loops. To address these challenges, various decoupling control techniques have been developed, involving both hardware and software-based approaches. One hardware solution proposed in [22], is a varying transformer winding configurations in order to reduce cross-coupling effects; however, restructuring transformer windings presents considerable design and manufacturing challenges. In [23], two additional switches per bidirectional port were introduced to reduce the cross-coupling effects, but this resulted in increased switching losses. Furthermore, in [24], a three-mode, three-port isolated DC-DC converter was proposed, utilising two DC relays for unidirectional decoupled power flow. However, mechanical relays can introduce reliability issues, switching delays, and shorten system lifespan, potentially affecting the overall performance of the converter. Another approach, as seen in [25–27], achieves inherent decoupling by reducing the primary-side leakage inductance to approximately 0.05 per unit, which is effective yet challenging in terms of complications in the transformer winding design. In [20,28], a resonant capacitor on the transformer's primary side was
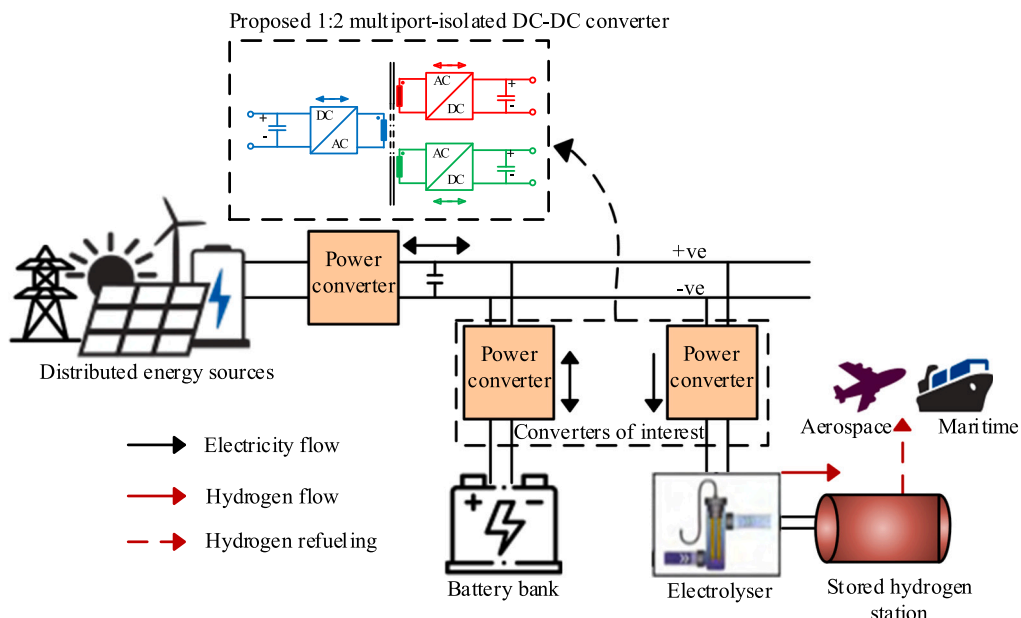

Fig. 1. Hydrogen energy storage system. Inset: 1:2 DC-DC multiport-isolated converter.

proposed to mitigate the cross-coupling effect, which could also potentially increase reactive power losses and complexities in terms of resonance tuning requirements. While these hardware-based strategies are relatively simple to implement, they come with trade-offs, including the addition or modification of components, which may lead to increased energy losses, reduced power density, and higher costs.

Software-based approaches are often preferred for their cost-effectiveness, as they eliminate the need for additional or modified hardware components. For example, a feedback linearisation-based controller implemented as a software-based decoupling control was used effectively to suppress cross-coupling effects in [29,30], though improper handling of the nonlinear inversion in the control loop may lead to performance degradation. Techniques like extended state observers, paired with advanced controls such as the sliding mode control and linear active disturbance rejection control have also been developed to detect and mitigate cross-coupling effects [31,32]; however, estimation errors can arise if controller gains are not optimally chosen, impacting control accuracy. An adaptive perturb-and-observe (P&O) controller, proposed to track the minimum point current, was developed in [33]. While this controller shows promising results, the P&O algorithm introduces additional computational burden on the system. Similarly, a single-input, single-output (SISO) system with different bandwidth selections was examined in [34]; while high-bandwidth loops enhances transient phase detection, aiding decoupling, lower-bandwidth loops exhibits poor anti-interference properties. In [35], a decoupling control technique using a proportional-derivative controller, model predictive control (MPC), and fuzzy compensation control achieved a reduced cross-coupling effect, but the combination's high computational demands may hinder real-time performance and increase implementation costs. Decoupling matrices are another common approach. A frequency domain modelling technique was applied in [36], to develop a decoupling matrix-based PI controller, yielding three lower-order AC equivalents, however, these AC equivalents may reintroduce measurement and control complexities, limiting practical implementation. Two independent control variables were introduced to the decoupling matrix, resulting in a phase difference matrix, as depicted in [37], nevertheless, the introduction and selection of the additional control variables in each loop added another layer of complication to the decoupling control design. The three-port active bridge described in [38,39] applies transmission line principles to analyse the converter power flow and uses a counter-reactive decoupling matrix to mitigate cross-coupling, although sensitivity to parameter variations may hinder consistent performance. In [40] an approach combining decoupling matrices, bandwidth selection, and feedforward current achieved effective decoupling, though its effectiveness was limited under asymmetrical loading across ports. A plant transfer matrix with a decoupling matrix, pre-calculated and stored in lookup tables (LUTs), was introduced in [41,42], and a comparative analysis of three of these decoupling matrices was conducted in [43], identifying the inverse decoupling matrix as superior in performance compared with others. While these software-based approaches demonstrate some success in mitigating cross-coupling effects, they often involve complex computations, particularly in larger systems. Additionally, their applicability is generally limited to specific operating regions, leading to incomplete decoupling, and the use of pre-calculated system matrices requires additional data storage in LUTs.

This paper proposes a novel software-based decoupling control technique to address these challenges. The proposed technique features a model reference-based decoupling control and a hybrid decoupling control (which combines the strengths of both model reference-based decoupling control and a decoupling matrix). The technique is designed to achieve excellent decoupling performance across a wider operating region. The main contributions of this paper are summarised as follows.

1. Proposing a novel software-based decoupling control technique that eliminates the reliance on look-up tables (LUTs), thereby significantly reducing memory requirements.
2. Developing a model reference-based decoupling control approach that minimises the error between the output of an ideal decoupling reference model and the actual plant, thereby enhancing control accuracy.
3. Proposing a hybrid decoupling control structure that integrates a decoupling matrix into the model reference-based framework, synergising their strengths to achieve robust decoupling and mitigate cross-coupling effects across a wider operating region.

This paper is divided into six sections. Section II briefly outlines the operating principles of a multiport-isolated DC-DC converter and derives the coupling terms. Based on this derivation, Section III presents an ideal decoupling reference model and the mathematical framework for developing the decoupling control. The results obtained from the simulations based on a three-port isolated converter (triple-active bridge converter) are discussed in Section IV. Section V presents the experimental results obtained using a proof-of-concept experimental setup to validate the decoupling performance, and the conclusions are provided in Section V1.

2. Operating principles of multiport-isolated DC-DC converter

An operational analysis of a three-port isolated converter (triple-active bridge converter) is provided in this section, and the cross-coupling effect is highlighted.

2.1. Analysis of TAB converter

For simplicity of analysis, Fig. 2 shows a three-port system with port 1 labelled as the BT port, port 2 as the DE (both represented by a voltage source), and port 3 labelled as the EL (represented by a resistive load). Negative power is the power supplied by a port, whereas positive power is the power absorbed by the port. The first bridge has switches S_1-S_4, while S_5-S_8 and S_9-S_{12} are the second and third bridges, respectively. Inductors $L_1, L'_2,$ and L'_3 are the leakage inductances, which are the major energy transfer elements. In addition, $i_1, i'_2,$ and i'_3 are the currents through the leakage inductances. The midpoint voltages are $u_1, u'_2,$ and u'_3, and the output voltages are $V_{BT}, V_{DE},$ and V'_{EL} respectively. The phase-shift angles (control inputs φ_2 and φ_3) are adjusted to enable power flow between the ports while maintaining the primary port at zero phase shift.

Calculating the equivalent inductance is crucial for the power flow between the ports. This requires transforming the star equivalent into the delta equivalent by superimposing the power transfer from each adjacent port and referring all circuit properties to the primary side, as shown in Fig. 3 [42].

Using cycle-by-cycle averaging, the power between ports can be expressed in (1):

$$P_{xy} = \frac{\varphi(\pi - \varphi)V_x V_y}{2\pi^2 f_s L_{xy}} \tag{1}$$

where, x and y represent 1, 2 or 3, indicating port numbers, V_x and V_y are the voltages of the two ports, f_s denotes the switching frequency, φ is the phase difference between the operating points, and L_{xy} is the inductance between the two ports in delta transformation.

The power flow in each port P_{BT}, P_{DE}, P_{EL} represents the total active output powers which are defined in (2) as seen in Fig. 3b.

$$P_{DE} = P_{23} + P_{21}, P_{EL} = -P_{23} - P_{13} \tag{2}$$
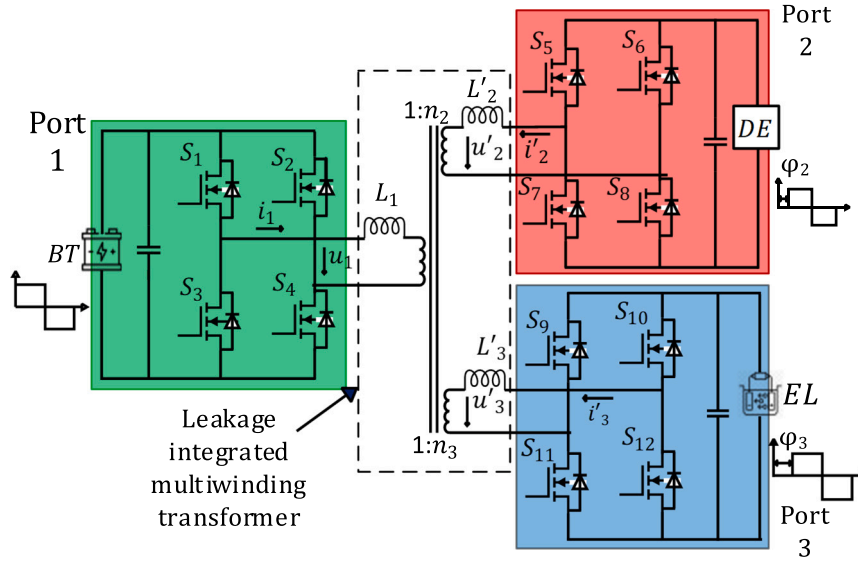
This can be further expressed as:

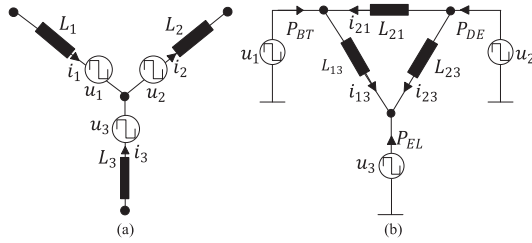**Fig. 2.** Topology of multiport-isolated DC-DC converter.

Fig. 3. Equivalent circuits of TAB converter: (a) star equivalent and (b) delta equivalent.

$$P_{DE} = \frac{\varphi_2(\varphi_2 - \pi)V_{BT}V_{DE}L_3 + (\varphi_3 - \varphi_2)(\varphi_2 - \varphi_3 - \pi)V_{DE}V_{EL}L_1}{2\pi^2 f_s A} \quad (3)$$

$$P_{EL} = \frac{\varphi_3(\pi - \varphi_3)V_{BT}V_{EL}L_2 + (\varphi_3 - \varphi_2)(\pi - \varphi_2 + \varphi_3)V_{DE}V_{EL}L_1}{2\pi^2 f_s A} \quad (4)$$

where,

$$A = L_1 L_2 + L_2 L_3 + L_1 L_3 \quad (5)$$

$$P_{BT} + P_{DE} + P_{EL} = 0 \quad (6)$$

Eqs. (3)-(6) show a nonlinear relationship between the output power and the control inputs.

2.2. Cross-coupling effect

To analyse the controllability of a multiport-isolated DC-DC converter, a simplified model is required that shows the impact of control inputs on output. State-space generalised average modelling, typically used to estimate the dynamics of a DC-DC converter, is challenging to apply to an isolated converter because the external inductor currents are taken as a state variable whose integral value over one switching cycle is zero. Consequently, the dynamic attributes of external inductors are ignored.

The output current from each port before filtering is expressed as in (7):

$$I_{DE} = \frac{P_{DE}}{V_{DE}}, I_{EL} = \frac{P_{EL}}{V_{EL}} \quad (7)$$

Considering the prefiltered currents as control variables, the derived

control-output relationship of the converter after linearisation around the operating region closest to the origin is given by (8), with *A* defined in (5), as illustrated in [44–46].

$$\begin{bmatrix} I_{DE} \\ I_{EL} \end{bmatrix} = \begin{bmatrix} \dfrac{4(V_{EL}L_1 + V_{BT}L_3)}{\pi^3 f_s A} & \dfrac{-4V_{EL}L_1}{\pi^3 f_s A} \\ \dfrac{-4V_{DE}L_1}{\pi^3 f_s A} & \dfrac{4(V_{DE}L_1 + V_{EL}L_2)}{\pi^3 f_s A} \end{bmatrix} \begin{bmatrix} \varphi_2 \\ \varphi_3 \end{bmatrix} \quad (8)$$

which, can be written conventionally as:

$$\begin{bmatrix} I_{DE} \\ I_{EL} \end{bmatrix} = \begin{bmatrix} G_{11} & G_{12} \\ G_{21} & G_{22} \end{bmatrix} \begin{bmatrix} \varphi_2 \\ \varphi_3 \end{bmatrix} \quad (9)$$

Therefore, the plant matrix is given by (10):

$$G = \begin{bmatrix} G_{11} & G_{12} \\ G_{21} & G_{22} \end{bmatrix} \quad (10)$$

Eq. (9) contains a 2×2 matrix with nonzero nondiagonal elements, indicating cross-coupling.

External inductors are conventionally used in TAB converters to compensate for the relatively low leakage inductance of multiwinding transformers. When the leakage inductance of the transformer is low, sufficient energy storage may not be provided. External inductors are added in such cases. The selection of these passive elements L_1, L'_2, and L'_3 is an essential aspect of the implementation of a TAB. According to the average power expressions in (3) and (4), the smaller the inductance value, the higher the average power flow. This may subsequently lead to a higher phase-shift angle when there is a steady power flow, and a larger current stress may be observed across the switching elements. An incorrect selection of inductance values could hinder the converter's ability to achieve the desired power transfer, potentially harm the switching elements, and have a significant influence on the decoupling control of the converter, as typified in (8). Any unsuitable variation in the values of inductive elements affects the computation of the decoupling structure of the converter.

3. Proposed decoupling control

The proposed decoupling control is explained in this section, which includes a novel model reference-based decoupling control technique. The novel model reference-based decoupling control is modified to a hybrid decoupling control which incorporates a decoupling matrix H in

the decoupling control structure.

3.1. Proposed model reference-based decoupling control

The degree of TAB coupling is determined by the ratio of non-diagonal elements (coupling terms) to diagonal elements. For complete decoupling, the coupling terms are equal to zero. However, this cannot be practically achieved. Hence, it is desirable to ensure that the TAB operates such that the nondiagonal elements approach zero.

$$\begin{bmatrix} I_{DE,ideal} \\ I_{EL,ideal} \end{bmatrix} = \begin{bmatrix} G_{11} & 0 \\ 0 & G_{22} \end{bmatrix} \begin{bmatrix} \varphi_2 \\ \varphi_3 \end{bmatrix} \tag{11}$$

Eq. (11) shows a diagonal matrix comprising uncoupling terms, which is equivalent to an ideal decoupling model. This model is subsequently employed as a reference model for decoupling control. Thus, the deviation of the TAB outputs from the ideal decoupling reference model (11) is used to mitigate the cross-coupling effect. The proposed model reference-based decoupling control schematics is shown in Fig. 4. Following (9), a proportional-integral (PI) controller is implemented to generate the intermediate control inputs, as follows:

$$\varphi_2 = K_P e_2 + \frac{K_I}{s} e_2 \tag{12}$$

$$\varphi_3 = K_P e_3 + \frac{K_I}{s} e_3 \tag{13}$$

where,

$$e_2 = I_{DE,ref} - I_{DE} \tag{14}$$

$$e_3 = I_{EL,ref} - I_{EL} \tag{15}$$

where, $I_{DE,ref}$ is the current reference in the *DE* port, which is represented by a voltage source, and $I_{EL,ref}$ is the current reference in the *EL* port, which is represented by a resistive load, for simplicity of analysis. Applying (9), (12, and 13) yields the actual current outputs from ports 2 and 3, respectively, as follows in (16) and (17):

$$I_{DE} = G_{11} \left(K_P e_2 + \frac{K_I}{s} e_2 \right) + G_{12} \varphi_3 \tag{16}$$

$$I_{EL} = G_{21} \varphi_2 + G_{22} \left(K_P e_3 + \frac{K_I}{s} e_3 \right) \tag{17}$$
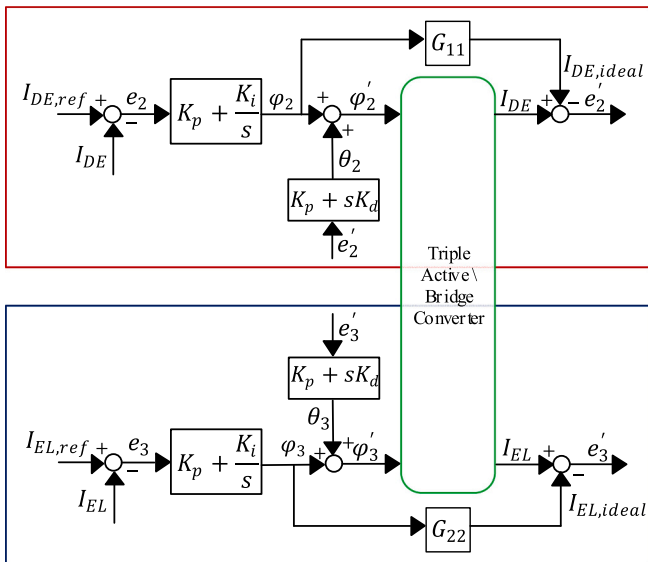

Fig. 4. Proposed model reference-based decoupling control schematics.

As shown in Fig. 4, the errors, e_2 and e_3, in (14) and (15) represent the error between the desired set-point value of the system and the output of the plant in each port. This error is kept minimal by using a simple PI controller. However, the ideal decoupling reference model will evolve based on the PI control laws (11)-(13) to yield:

$$I_{DE,ideal} = G_{11} \left(K_P e_2 + \frac{K_I}{s} e_2 \right) \tag{18}$$

$$I_{EL,ideal} = G_{22} \left(K_P e_3 + \frac{K_I}{s} e_3 \right) \tag{19}$$

The outputs of the ideal decoupling reference model are compared with the actual current outputs of the TAB at each port. From (16) − (19), the difference between the ideal decoupling reference model output and plant output is related to the coupling terms.

The error, e_2' and e_3', as seen in (20), (21) and Fig. 4 is used to suppress the coupling terms in the system, which is similar to an internal disturbance that affects the precise independent control of each loop.

$$e_2' = I_{DE} - I_{DE,ideal} \tag{20}$$

$$e_3' = I_{EL} - I_{EL,ideal} \tag{21}$$

Consequently, a simple proportional (P) or proportional-derivative (PD) controller is sufficient for the control. In this paper, a PD is used for the error, e_2' and e_3' to mitigate the sensitivity of the system to internal disturbances, and to enhance the robustness of the control system. However, an excessive derivative gain can render the system sensitive to measurement noise. Therefore, a proper and careful tuning of the controller is necessary.

Based on the deviation of the TAB output from the ideal decoupling reference model, additional control signals θ_2 and θ_3 are generated, as shown in (22) and (23), respectively.

$$\theta_2 = e_2' \left(K_p + s K_d \right) \tag{22}$$

$$\theta_3 = e_3' \left(K_p + s K_d \right) \tag{23}$$

This limits the influence of the coupling terms on the intermediate control inputs φ_2 and φ_3. By driving the system to be as close as possible to the ideal decoupling reference model, the intermediate control inputs are modified to an actual control input. The resulting actual control inputs are given as:

$$\varphi_2' = \varphi_2 + \theta_2 \tag{24}$$

$$\varphi_3' = \varphi_3 + \theta_3 \tag{25}$$

Therefore, the actual control inputs (24) and (25) not only help achieve tracking control but also ensure mitigation of the cross-coupling effect.

3.2. Proposed hybrid decoupling control

To ensure a more robust system, a decoupling matrix *H* is incorporated into the model reference-based decoupling control technique, as shown in Fig. 5. The implemented decoupling matrix is the inverse of matrix *G*, as given by (26):

$$H = G^{-1} = \frac{1}{G_{11}G_{22} - G_{12}G_{21}} \begin{bmatrix} G_{22} & -G_{12} \\ -G_{21} & G_{11} \end{bmatrix} \tag{26}$$

Hence, considering the decoupling matrix, the modified ideal decoupling reference model with uncoupling terms is given in (27).

$$\begin{bmatrix} I_{DE,ideal} \\ I_{EL,ideal} \end{bmatrix} = \begin{bmatrix} G_{11}H_{11} & 0 \\ 0 & G_{22}H_{22} \end{bmatrix} \begin{bmatrix} r_2 \\ r_3 \end{bmatrix} \tag{27}$$

A PI controller is implemented to derive the medium variations r_2 and r_3, as depicted in Fig. 5, calculated in (28) and (29)
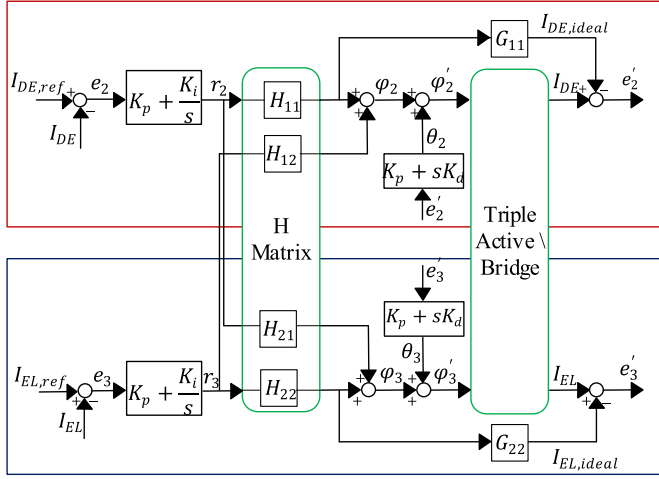
Fig. 5. Proposed hybrid decoupling control schematics.

$$r_2 = K_P e_2 + \frac{K_I}{s} e_2 \tag{28}$$

$$r_3 = K_P e_3 + \frac{K_I}{s} e_3 \tag{29}$$

where, e_2 and e_3 follows from the same expression (14) and (15).

Consequently, the modified intermediate control inputs φ_2 and φ_3, are generated as follows in (30) and (31):

$$\varphi_2 = H_{11} r_2 + H_{12} r_3 \tag{30}$$

$$\varphi_3 = H_{21} r_2 + H_{22} r_3 \tag{31}$$

Thus, the modified control-output relationship after simplification is expressed as in (32) and (33):

$$I_{DE} = G_{11} H_{11} \left(K_P e_2 + \frac{K_I}{s} e_2 \right) + (G_{11} H_{12} r_3 + G_{12} \varphi_3) \tag{32}$$

$$I_{EL} = (G_{21} \varphi_2 + G_{22} H_{21} r_2) + G_{22} H_{22} \left(K_P e_3 + \frac{K_I}{s} e_3 \right) \tag{33}$$

The modified ideal decoupling reference model will evolve based on the medium variations by substituting (28) and (29) into (27) to yield (34) and (35).

$$I_{DE,ideal} = G_{11} H_{11} \left(K_P e_2 + \frac{K_I}{s} e_2 \right) \tag{34}$$

$$I_{EL,ideal} = G_{22} H_{22} \left(K_P e_3 + \frac{K_I}{s} e_3 \right) \tag{35}$$

Following mathematically (20) − (23) and as shown in Fig. 5, implementing a PD controller, the actual control inputs that will achieve set point tracking and ensure mitigation of cross-coupling effect are given as follows in (36) and (37):

$$\varphi'_2 = \varphi_2 + \theta_2 \tag{36}$$

$$\varphi'_3 = \varphi_3 + \theta_3 \tag{37}$$

The theoretical analysis of the proposed decoupling controller highlights its effectiveness in mitigating cross-coupling effects. However, practical implementation requires attention to a few key aspects. For instance, this decoupling control technique introduces additional controller gains, which, while beneficial for increased flexibility, require precise tuning to achieve optimal performance. Tuning the PD controller, particularly the derivative gain, can influence electromagnetic interference (EMI). To balance improved control performance with

noise suppression, cautious tuning of the derivative term is recommended to minimise any high-frequency noise that could contribute to EMI. Additionally, the converter employs MOSFETs as switching devices, which are selected for their faster switching speeds and lower switching losses compared to IGBTs. In terms of thermal management, appropriately sized heat sinks were integrated to ensure efficient heat dissipation and reliable operation of the MOSFETs. These considerations collectively enhance the practical feasibility and robustness of the proposed decoupling controller, making it a reliable solution for mitigating cross-coupling effects in multiport isolated DC-DC converters.

4. Simulation results

To verify the effectiveness of the proposed decoupling control technique, simulations are conducted using the specifications listed in Table 2. The circuit is modelled in the SIMULINK/MATLAB software environment, with the control schematics implemented, as shown in Fig. 4 and Fig. 5. Controller gains are selected through a trial-and-error approach.

The performance of the proposed model reference-based decoupling control and hybrid decoupling control techniques is demonstrated in Fig. 6 and Fig. 7, respectively. These figures highlight the controllers' effectiveness in mitigating cross-coupling effects—observed as disturbances in the form of power deviations (overshoot or undershoot) at the corresponding port in response to intended or unintended changes in the power supply or power absorbed by other ports—and in maintaining stable power transfer across different ports under worst case conditions. Two scenarios are simulated to illustrate controller performance under step changes in power transfer:

1. Scenario 1 (Fig. 6a and Fig. 7a) examines changes in the power supply at the DE port (P_{DE}). Step changes are applied at 0.05 s, 0.1 s, and 0.15 s, with transitions from −200 W to −1000 W, −1000 W to −600 W, and − 600 W to −750 W, respectively, while maintaining a constant power absorption of 1000 W at the EL port (P_{EL}). The BT port (P_{BT}) acts as a slack bus, adjusting to balance power transfer.
2. Scenario 2 (Fig. 6b and Fig. 7b) examines changes in the power absorbed at the EL port (P_{EL}). Step changes occur at the same time intervals, with the power absorbed by P_{EL} transitioning from 0 W to 1000 W, then from 1000 W to 350 W, and finally from 350 W to 100 W, while maintaining a constant power supply of 1000 W at the DE

Table 2
Circuit design parameters.

| Description	Symbol	Unit	Ports		
			#1	#2	#3
Voltage Rating	V_{BT}, V_{DE}, V_{EL}	V	560	46	73
Leakage Inductance	L_1, L'_2, L'_3	µH	780	4.992	13.18
Switching frequency	f_s	kHz	15	15	15
Transformer Turns Ratio	n_2, n_3	–	1	0.08	0.13
Controller Gains	K_p	–	–	15	10
(Model reference-based decoupling control, hybrid decoupling control, inverse matrix decoupling control, and control without decoupling methodology)	K_i	–	–	6000	8000
Model reference-based decoupling control, hybrid decoupling control	K_d	–	–	0.001	0.00085
	K_p	–	–	0.01	0.001
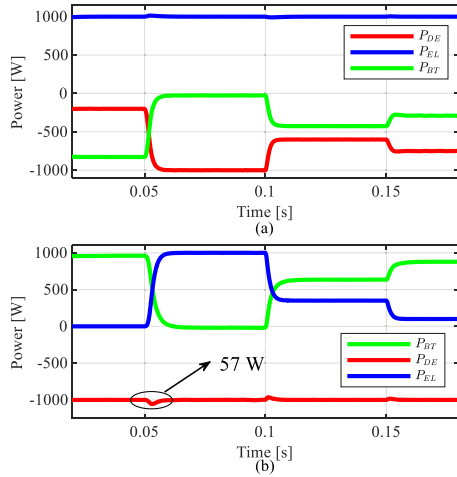
Fig. 6. Power transfer between ports using the proposed model reference-based decoupling control: (a) power absorbed by the EL when step changes are applied to the power supply by the DE and BT ports, and (b) power supply by the DE ports when step changes are applied to the power absorbed in the EL and BT ports.
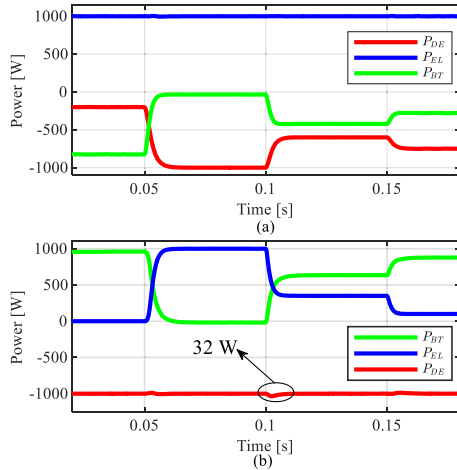

Fig. 7. Power transfer between ports using the proposed hybrid decoupling control: (a) power absorbed by the EL when step changes are applied to the power supply by the DE and BT ports, and (b) power supply by the DE ports when step changes are applied to the power absorbed in the EL and BT ports.

port (P_{DE}). The BT port (P_{BT}) continues to act as the slack bus in this scenario.

Using the model reference-based decoupling control shown in Fig. 6, the controller minimises the cross-coupling effect by comparing the output of the decoupling reference model to the plant output. This comparison allows the controller to interpret the error as the coupling

term and suppress it. As shown in Fig. 6a (scenario 1), this technique results in negligible power overshoot from the nominal value at the EL port. In scenario 2 (Fig. 6b), the model reference-based control reduces the cross-coupling effect, with a maximum undershoot of 6 % from the nominal value occurring at the 0.05 s step change.

In comparison, the proposed hybrid decoupling control in Fig. 7 further improves performance with a negligible power overshoot or undershoot in scenario 1 (Fig. 7a). In scenario 2 (Fig. 7b), the hybrid decoupling control shows enhanced robustness, with the worst case power undershoot reduced to 3 % at the 0.1 s step change.

Table 3 provides a qualitative comparative overview of decoupling control techniques for multiport-isolated DC-DC converters from both software and hardware perspectives, highlighting the key improvements offered by the proposed hybrid decoupling control. To further demonstrate the superiority of the proposed method, it is evaluated through simulations alongside a matrix-based decoupling control—the conventional inverse matrix decoupling control illustrated in [42] and a control approach without decoupling. The results are as shown in Fig. 8 and Fig. 9 for each scenario. Fig. 8 and Fig. 9 specifically extract the response of the ports susceptible to power overshoot and undershoot due to step changes on other ports, as illustrated in Figs. 6 and 7, for each controller type, providing a clearer view.

In scenario 1, the proposed hybrid decoupling control exhibits excellent decoupling, with negligible power overshoot/undershoot, as shown in Fig. 8a. In contrast, the inverse matrix decoupling control experiences a worst case power undershoot of 3 % from the nominal value at the 0.05 s step change, as shown in Fig. 8b. Meanwhile, the control without decoupling methodology demonstrates a worst case power overshoot of 8 % at the 0.05 s step change, as seen in Fig. 8c.

Furthermore, in scenario 2, the performance difference is even more pronounced. The proposed hybrid decoupling control technique more effectively suppresses the cross-coupling effect, with a reduced power undershoot of only 3 % at the 0.1 s step change, as depicted in Fig. 9a. Whereas, as shown in Fig. 9b and Fig. 9c, the inverse matrix decoupling control and the control without decoupling methodology experience worst case power undershoots of 8 % and 9 %, respectively.

In terms of efficiency, the conduction losses in the system are calculated using $P_c = I_{rms}^2 R_{on}$ where, R_{on} represents the on-state resistance of each switch. These losses are directly influenced by the root-mean-square current through the switches. With the proposed hybrid decoupling control, the system achieves an end-to-end efficiency of 91.80 %, compared to 89.75 % for the conventional inverse matrix decoupling control and 88 % for the control without decoupling. These results were obtained under a constant 1000 W power supply with step changes applied to the EL port, as shown in Fig. 7b, and replicated across all decoupling controllers under investigation. This scenario represents the worst-case operating condition, highlighting the robustness of the proposed control technique. The present study employs single-phase shift control, which is susceptible to high circulating currents, leading to higher losses and limiting the extent of efficiency improvement. Future studies will explore the integration of additional phase shift control strategies to minimise circulating currents within the converter. This approach aims to further enhance the efficiency of the multiport-

Table 3
Overview of Multiport-isolated DC-DC Converter Decoupling Techniques.

| Details of operation	Hardware solution		Software solution		
	[23]	[20]	[31]	[42]	Proposed hybrid decoupling control
Additional component	Two switches /low primary inductance	Resonant Capacitor	None	None	None
Estimation error	None	None	Yes	None	None
Ease of implementation	Medium	Low	High	Medium	Medium
Extra data storage	Low	Low	Medium	High	Low
Power operational region	Medium	Narrow	Medium	Narrow	Wide
Hardware Complexity	High	Medium	Low	Low	Low
Converter Configuration	Symmetric	Asymmetric	Symmetric/ Asymmetric	Asymmetric	Asymmetric
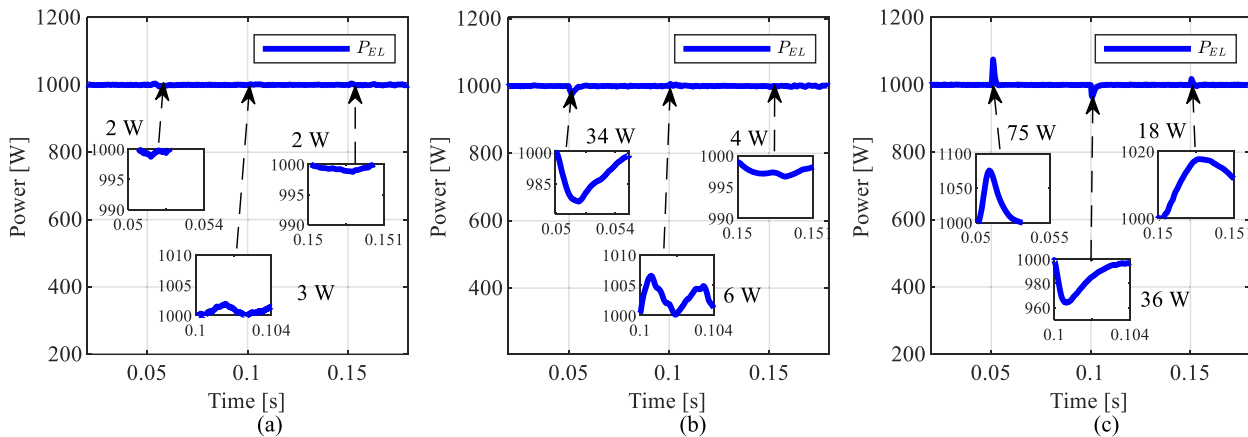
Fig. 8. Power absorbed by the EL when step changes are applied to the power supply in the DE and BT ports for (a) the proposed hybrid decoupling control, (b) inverse matrix decoupling control, and (c) control without decoupling methodology.
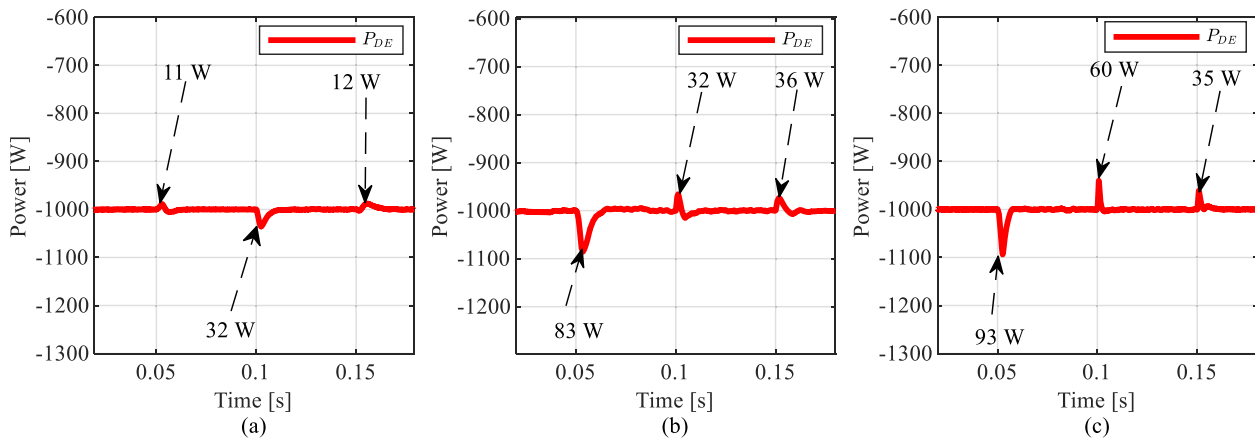

Fig. 9. Power supply from the DE port when step changes are applied to the power absorbed in the EL and BT ports for (a) hybrid decoupling control, (b) inverse matrix decoupling control, and (c) control without decoupling methodology.

isolated DC-DC converter.

Nevertheless, these results demonstrate the superior performance of the hybrid decoupling control technique in reducing cross-coupling effects and maintaining stable power levels across ports under varying conditions.

5. Experimental validation

To further validate the proposed controller and align the theoretical analysis with the experimental results, a proof-of-concept circuit, as depicted in Fig. 10 is developed. The parameters of the experimental circuit are scaled down from those used in simulations. The rated power for this experimental setup is 380 W, operating at a switching frequency of 20 kHz. The leakage inductances of L_1, L_2 and L_3 are 50 µH, 48 µH and 49 µH respectively. The transformer core material utilised is N87, with dimensions R 50/30/20, with a turn ratio of 17:15:11.

The experiment was conducted to imitate scenario 2 of the simulation, observing the impact of the EL port variation while keeping the DE port supplying a steady current and the BT port serving as the slack bus to compensate for the changes and maintain the system balance. Fig. 11 illustrates the experiment conducted using three control techniques: the proposed hybrid decoupling control, the conventional inverse matrix decoupling control as illustrated in [42], and control without decoupling methodology. The current in the EL varied from 2.8 A to 4.2 A, marking a 50 % rise in load demand. This variation led to a proportional change in the BT current, stepping it from 0.4 A to 3.6 A. Fig. 11a, indicates a
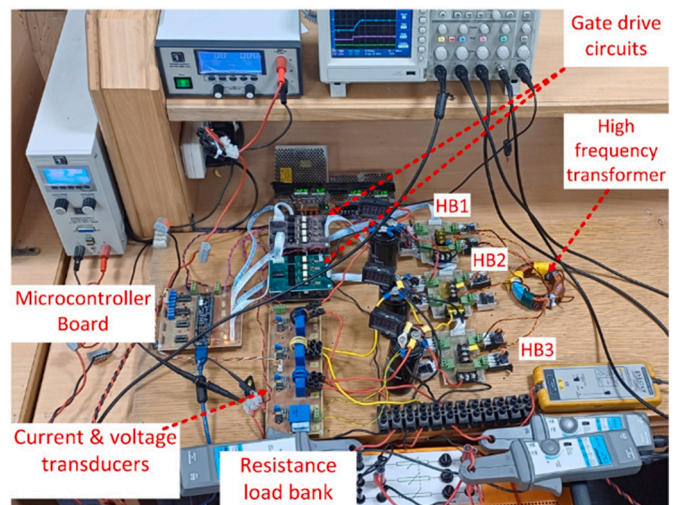

Fig. 10. Experimental test rig.

deviation of 0.1 A in the DE port, representing a 5 % deviation from the nominal value with the hybrid decoupling control technique. In contrast, with the inverse matrix decoupling control and control without decoupling methodology shown in Fig. 11b and Fig. 11c, respectively,
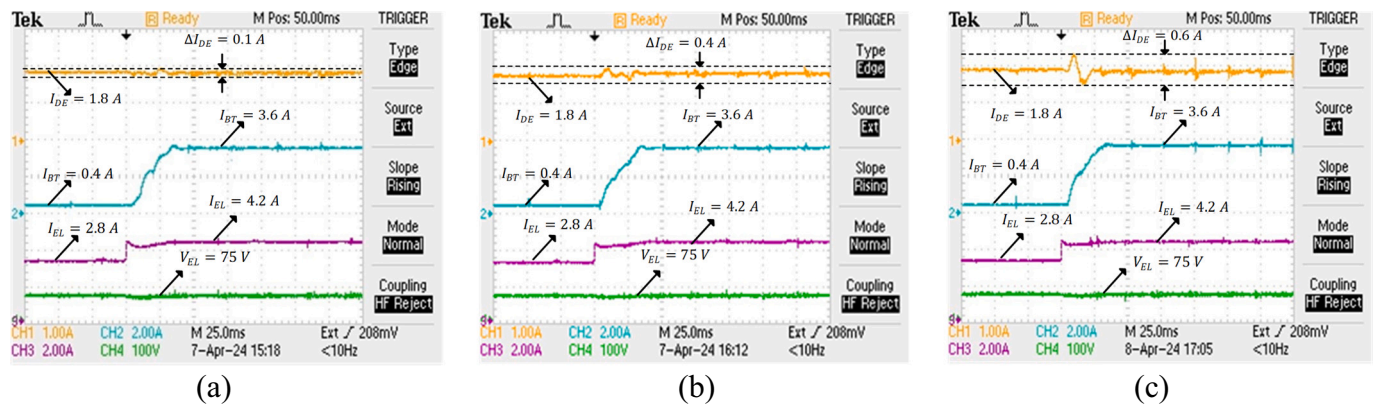
Fig. 11. Experimental results showing power supply from the DE port when there is an EL port change from 2.8 A to 4.2 A (a) hybrid decoupling control, (b) inverse matrix decoupling control, and (c) control without decoupling methodology.

there are deviations of 0.4 A and 0.6 A, corresponding to 22 % and 33 % deviations from the nominal value.

6. Conclusion

A model reference-based decoupling control has been proposed to mitigate the cross-coupling effect associated with multiwinding transformers in multiport isolated DC-DC converters for hydrogen energy storage system applications. Using an ideal decoupling reference model, a mathematical formulation was developed that addresses and suppresses cross-coupling effects by minimising the error between output of the model and the actual plant. Additionally, a hybrid decoupling control technique, which integrates a decoupling matrix into the model reference-based decoupling structure, showed superior decoupling control performance across the two simulated scenarios, with a consistent response under variable load conditions. Compared with the conventional inverse matrix decoupling control and control without decoupling methodology, the proposed method performs well in a wider operating region, achieving a worst-case power deviation of only 3 %, whereas conventional methods have power deviations of approximately 8–10 %. Furthermore, the proposed technique achieved a 2.05 % efficiency improvement over conventional inverse matrix decoupling control in the worst-case scenario. A 380 W proof-of-concept validates the efficacy of the proposed decoupling control technique, demonstrating its practical feasibility. These results underscore the potential of the proposed technique for improving decoupling control in HESS applications by improving on the limitations associated with conventional decoupling control techniques. Future research will focus on a comprehensive analysis of the converter's power losses and efficiency, with an exploration of additional phase shift modulation techniques to further enhance performance.

CRediT authorship contribution statement

Oyedotun E. Oyewole: Writing – original draft, Validation, Software, Methodology, Formal analysis, Conceptualization. **Ali A. Abdelaziz:** Writing – review & editing, Validation, Supervision. **Ibrahim Abdelsalam:** Visualization, Validation, Investigation. **Eugene Bari:** Resources. **Khaled H. Ahmed:** Writing – review & editing, Validation, Supervision.

Declaration of competing interest

The authors declare that they have no known competing financial interests or personal relationships that could have appeared to influence the work reported in this paper.

Data availability

No data was used for the research described in the article.

References

[1] F. Samimi, M. Ghiyasiyan-Arani, M. A. Mahdi, L. S. Jasim, A. F. Zonouz, and M. Salavati-Niasari, "Preparation, microstructural characteristics, and electrochemical properties of cobalt molybdate nanocomposites as electrode material for hydrogen storage," Journal of Energy Storage, vol. 85, p. 111027, 2024/04/30/ 2024, doi:https://doi.org/10.1016/j.est.2024.111027.

[2] M.J.B. Kabeyi, O.A. Olanrewaju, Sustainable energy transition for renewable and low carbon grid electricity generation and supply, (in English), Frontiers in Energy Research, Review 9 (2022), https://doi.org/10.3389/fenrg.2021.743114, 2022-March-24.

[3] M. Nooman AlMallahi, Y. Al Swailmeen, M. Ali Abdelkareem, A. Ghani Olabi, and M. Elgendi, "A path to sustainable development goals: a case study on the thirteen largest photovoltaic power plants," Energy Convers. Manag.: X, vol. 22, p. 100553, 2024/04/01/ 2024, doi:https://doi.org/10.1016/j.ecmx.2024.100553.

[4] Z. Heydariyan, M. Salavati-Niasari, and R. Monsef, "Preparation and investigation of TbCrO3/montmorillonite-K10 nanocomposite electrode for electrochemical hydrogen storage application," Fuel, vol. 372, p. 132177, 2024/09/15/ 2024, doi:https://doi.org/10.1016/j.fuel.2024.132177.

[5] A.S. Abdulbaqi, et al., Innovative control strategies for dynamic load Management in Smart Grid Techniques Incorporating Renewable Energy Sources, KHWARIZMIA 07/18 2023 (2023) 73–83, https://doi.org/10.70470/KHWARIZMIA/2023/007.

[6] S. Zinatloo-Ajabshir, Z. Salehi, O. Amiri, and M. Salavati-Niasari, "Simple fabrication of Pr2Ce2O7 nanostructures via a new and eco-friendly route; a potential electrochemical hydrogen storage material," J. Alloys Compd., vol. 791, pp. 792–799, 2019/06/30/ 2019, doi:https://doi.org/10.1016/j.jallcom.2019.04.005.

[7] M. Awad et al., "A review of water electrolysis for green hydrogen generation considering PV/wind/hydropower/geothermal/tidal and wave/biogas energy systems, economic analysis, and its application," Alex. Eng. J., vol. 87, pp. 213–239, 2024/01/01/ 2024, doi:https://doi.org/10.1016/j.aej.2023.12.032.

[8] G. Deng et al., "Electrochemical properties and hydrogen storage mechanism of perovskite-type oxide LaFeO3 as a negative electrode for Ni/MH batteries," Electrochim. Acta, vol. 55, no. 3, pp. 1120–1124, 2010/01/01/ 2010, doi:https://doi.org/10.1016/j.electacta.2009.09.078.

[9] P. Breeze, Chapter 8 - Hydrogen Energy Storage, in: P. Breeze (Ed.), Power System Energy Storage Technologies, Academic Press, 2018, pp. 69–77.

[10] L. Wan, W. Zhang, and Z. Xu, "Overview of Key Technologies and Applications of Hydrogen Energy Storage in Integrated Energy Systems," in 2020 12th IEEE PES Asia-Pacific Power and Energy Engineering Conference (APPEEC), 20–23 Sept 2020 2020, pp. 1–5, doi:https://doi.org/10.1109/APPEEC48164.2020.9220454.

[11] S. Furfari and A. Clerici, "Green hydrogen: the crucial performance of electrolysers fed by variable and intermittent renewable electricity," The European Physical Journal Plus, vol. 136, no. 5, p. 509, 2021/05/08 2021, doi:https://doi.org/10.1140/epjp/s13360-021-01445-5.

[12] Y. Mona Ghassan, "optimal control of dynamical systems using Calculus of variations," *Babylonian*, Journal of Mathematics 01/28 2023 (2023) 1–6, https://doi.org/10.58496/BJM/2023/001.

[13] A. Andrijanovits, ""New Converter Topologies for Integration of Hydrogen Based Long-Term Energy Storages to Renewable Energy Systems," PhD, Department of Electrical Engineering, Tallinn University of Technology, 2013, 2013.

[14] J. Li, Q. Luo, T. Luo, D. Mou, M. Liserre, Efficiency optimization scheme for isolated triple active bridge DC–DC converter with full soft-switching and minimized RMS current, IEEE Trans. Power Electron. 37 (8) (2022) 9114–9128, https://doi.org/10.1109/tpel.2022.3157443.

[15] D. Vinnikov, A. Andrijanovits, I. Roasto, and T. Jalakas, "Experimental study of new integrated DC/DC converter for hydrogen-based energy storage," in *2011 10th International Conference on Environment and Electrical Engineering*, 8–11 May 2011 2011, pp. 1–4, doi:https://doi.org/10.1109/EEEIC.2011.5874667.

[16] D. Guilbert, S. M. Collura, and A. Scipioni, "DC/DC converter topologies for electrolyzers: state-of-the-art and remaining key issues," Int. J. Hydrog. Energy, vol. 42, no. 38, pp. 23966–23985, 2017/09/21/ 2017, doi:https://doi.org/10.1016/j.ijhydene.2017.07.174.

[17] G. Oroumi et al., "Achieving new insights on rational design and application of double perovskite Y2CrMnO6 nanostructures as potential materials for electrochemical hydrogen storage performance," Journal of Energy Storage, vol. 85, p. 111161, 2024/04/30/ 2024, doi:https://doi.org/10.1016/j.est.2024.111161.

[18] M. Jafari, Z. Malekjamshidi, G. Platt, J.G. Zhu, "a Multi-Port Converter Based Renewable Energy System for Residential Consumers of Smart Grid," *IECON2015 Yokohama*, November 9–12, 2015.

[19] Y. A. Harrye, K. H. Ahmed, and A. A. Aboushady, "DC fault isolation study of bidirectional dual active bridge DC/DC converter for DC transmission grid application," *IECON 2015 - 41st Annual Conference of the IEEE Industrial Electronics Society*, pp. 3193–3198, 2015, doi:https://doi.org/10.1109/IECON.2015.7392592.

[20] P. Wang, X. Lu, W. Wang, D. Xu, Hardware decoupling and autonomous control of series-resonance-based three-port converters in DC microgrids, IEEE Trans. Ind. Appl. 55 (4) (2019) 3901–3914, https://doi.org/10.1109/TIA.2019.2906112.

[21] H. Dai, W. Tang, Modeling and simulation in fuel cells, in: R. Gupta (Ed.), Handbook of Energy Materials, Springer Nature Singapore, Singapore, 2022, pp. 1–45.

[22] S. Dey, C. Reece, O.P. Irabor, A. Mallik, Comparative analysis and optimization of triple active bridge transformer configuration with Integrable leakage inductance, IEEE Journal of Emerging and Selected Topics in Power Electronics 11 (5) (2023) 5102–5119, https://doi.org/10.1109/JESTPE.2023.3298894.

[23] P. Koohi et al., "A Hardware-Based Bidirectional Power Flow Decoupling Approach for Multi-Active-Bridge Converters," in *2023 IEEE Int. Conf. Electr. Syst. Aircr. Railw. Sh. Propuls. Road Veh. Int. Transp. Electrif. Conf. ESARS-ITEC*, 29–31 March 2023, pp. 1–7, doi:https://doi.org/10.1109/ESARS-ITEC57127.2023.10114906.

[24] M. A. Dev, K. T. H. Babu, and P. F. Beevi, "Three Mode Three-Port Isolated DC/DC Converter With Dual Fast Charging Port," in *2022 International Conference on Futuristic Technologies in Control Systems & Renewable Energy (ICFCR)*, 21–22 July 2022 2022, pp. 1–6, doi:https://doi.org/10.1109/ICFCR54831.2022.9893609.

[25] S. Bandyopadhyay, P. Purgat, Z. Qin, P. Bauer, A multiactive bridge converter with inherently decoupled power flows, IEEE Trans. Power Electron. 36 (2) (2021) 2231–2245, https://doi.org/10.1109/tpel.2020.3006266.

[26] D. U. Kim, B. Byen, B. Jeong, and S. Kim, "Design of Triple-Active-Bridge Converter with Inherently Decoupled Power Flows," in *2022 24th European Conference on Power Electronics and Applications (EPE'22 ECCE Europe)*, 5–9 Sept. 2022 2022, pp. 1–9.

[27] A. Panchbhai, R. Ranjan, G. Chilkalpudi, and A. Kumar, "Power Decoupling Using Inductor In Triple Active Bridge," in *2023 International Conference on Power, Instrumentation, Control and Computing (PICC)*, 19–21 April 2023 2023, pp. 1–5, doi:https://doi.org/10.1109/PICC57976.2023.10142490.

[28] P. Wang, W. Wang, D. Xu, and X. Lu, "A hardware decoupling method for series-resonance-based isolated three-port DC/DC converters," in *2018 IEEE Applied Power Electronics Conference and Exposition (APEC)*, 4–8 March 2018 2018, pp. 1585–1590, doi:https://doi.org/10.1109/APEC.2018.8341228.

[29] V. Repecho, J.M. Olm, R. Griñó, A. Dòria-Cerezo, E. Fossas, Modelling and nonlinear control of a magnetically coupled multiport DC-DC converter for

[30] J. M. Olm, E. Fossas, V. Repecho, A. Dória-Cerezo, and R. Griñó, "Feedback linearizing control of a magnetically coupled multiport dc-dc converter for automotive applications," in *IECON 2019 - 45th Annual Conference of the IEEE Industrial Electronics Society*, 14–17 Oct. 2019 2019, vol. 1, pp. 2688–2692, doi:https://doi.org/10.1109/IECON.2019.8927831.

[31] S. Gong, et al., Sliding mode control-based decoupling scheme for quad-active bridge DC–DC converter, IEEE Journal of Emerging and Selected Topics in Power Electronics 10 (1) (2022) 1153–1164, https://doi.org/10.1109/jestpe.2021.3096228.

[32] S. Bandyopadhyay, Z. Qin, P. Bauer, Decoupling control of multiactive bridge converters using linear active disturbance rejection, IEEE Trans. Ind. Electron. 68 (11) (2021) 10688–10698, https://doi.org/10.1109/tie.2020.3031531.

[33] O.M. Hebala, A.A. Aboushady, K.H. Ahmed, I. Abdelsalam, Generalized active power flow controller for multiactive bridge DC–DC converters with minimum-current-point-tracking algorithm, IEEE Trans. Ind. Electron. 69 (4) (2022) 3764–3775, https://doi.org/10.1109/tie.2021.3071681.

[34] H. Tao, A. Kotsopoulos, J.L. Duarte, M.A.M. Hendrix, Transformer-coupled multiport ZVS bidirectional DC–DC converter with wide input range, IEEE Trans. Power Electron. 23 (2) (2008) 771–781, https://doi.org/10.1109/TPEL.2007.915129.

[35] A.H.A. Adam, et al., Power decoupling enhancement of a triple active bridge converter with feedforward compensation based on model predictive control and fuzzy logic controller in DC microgrid systems, IEEE Access 12 (2024) 140310–140328, https://doi.org/10.1109/ACCESS.2024.3469815.

[36] I. Biswas, D. Kastha, P. Bajpai, Small signal modeling and decoupled controller Design for a Triple Active Bridge Multiport DC–DC converter, IEEE Trans. Power Electron. 36 (2) (2021) 1856–1869, https://doi.org/10.1109/tpel.2020.3006782.

[37] I. Biswas, D. Kastha, and P. Bajpai, "Isolated Multiport Converter for fuel Cell and Energy Storage systems for DC Microgrid," in *2017 14th IEEE India Council International Conference (INDICON)*, 15–17 Dec. 2017 2017, pp. 1–6, doi:https://doi.org/10.1109/INDICON.2017.8487536.

[38] A. Chandwani, A. Mallik, and A. M. Kannan, "A Novel Decoupled Control Scheme for Phase Controlled Triple Active Bridge," presented at the IECON 2021 – 47th Annual Conference of the IEEE Industrial Electronics Society, 2021.

[39] A. Chandwani, A. Mallik, Phase-duty modulated loop decoupling and design optimization for a triple active bridge converter for light electric vehicle charging, IEEE Journal of Emerging and Selected Topics in Industrial Electronics 4 (1) (2023) 357–367, https://doi.org/10.1109/JESTIE.2022.3179942.

[40] G. Buticchi, L.F. Costa, D. Barater, M. Liserre, E.D. Amarillo, A quadruple active bridge converter for the storage integration on the more electric aircraft, IEEE Trans. Power Electron. 33 (9) (2018) 8174–8186, https://doi.org/10.1109/TPEL.2017.2781258.

[41] K.O. Bempah, K.-W. Heo, J.-H. Jung, Power flow decoupling method of triple-active-bridge converter for islanding mode operation in DC microgrid systems, Journal of Power Electronics 23 (1) (2022) 58–67, https://doi.org/10.1007/s43236-022-00528-5.

[42] C. Zhao, S.D. Round, J.W. Kolar, An isolated three-port bidirectional DC-DC converter with decoupled power flow management, IEEE Trans. Power Electron. 23 (5) (2008) 2443–2453, https://doi.org/10.1109/tpel.2008.2002056.

[43] O.E. Oyewole, K.H. Ahmed, "Comparative Analysis of Decoupling Control Methods for Multiport-Isolated Bidirectional DC-DC Converter with Hydrogen Storage System Integration," Presented at the 2023 11th International Conference on Smart Grid (icSmartGrid), 2023.

[44] O. E. Oyewole, A. A. Abdelaziz, I. A. Jimoh, E. Bari, and K. H. Ahmed, "Optimised linear active disturbance rejection control of multiport-isolated DC-DC converter for hydrogen energy storage system integration," Alex. Eng. J., vol. 102, pp. 159–168, 2024/09/01/ 2024, doi:https://doi.org/10.1016/j.aej.2024.05.107.

[45] K. Nishimoto, Y. Kado, K. Wada, Implementation of decoupling power flow control system in triple active bridge converter rated at 400V, 10kW, and 20kHz, IEEJ J. Ind. Appl. 7 (5) (2018) 410–415, https://doi.org/10.1541/ieejjia.7.410.

[46] S. Rahman, I. Khan, S. Dey, A. Mallik, Triple-active bridge-based dynamic power balancing solution for minimizing overdesigning in military aircraft power system, IEEE Trans. Veh. Technol. (2023) 1–11, https://doi.org/10.1109/TVT.2023.3323538.